

Development of Edgeless n-on-p Planar Pixel Sensors for future ATLAS Upgrades

M. BOMBEN^{a,*}, A. BAGOLINI^b, M. BOSCARDIN^b, L. BOSISIO^c,
G. CALDERINI^{a,d}, J. CHAUVEAU^a, G. GIACOMINI^b, A. LA ROSA^e,
G. MARCHIORI^a, N. ZORZI^b

^a*Laboratoire de Physique Nucleaire et de Hautes Énergies (LPNHE)
Paris, France*

^b*Fondazione Bruno Kessler, Centro per i Materiali e i Microsistemi (FBK-CMM)
Povo di Trento (TN), Italy*

^c*Università di Trieste, Dipartimento di Fisica and INFN, Trieste, Italy*

^d*Dipartimento di Fisica E. Fermi, Università di Pisa, and INFN Sez. di Pisa, Pisa, Italy*

^e*Section de Physique (DPNC), Université de Genève, Genève, Switzerland*

Abstract

The development of n-on-p “edgeless” planar pixel sensors being fabricated at FBK (Trento, Italy), aimed at the upgrade of the ATLAS Inner Detector for the High Luminosity phase of the Large Hadron Collider (HL-LHC), is reported. A characterizing feature of the devices is the reduced dead area at the edge, achieved by adopting the “active edge” technology, based on a deep etched trench, suitably doped to make an ohmic contact to the substrate. The project is presented, along with the active edge process, the sensor design for this first n-on-p production and a selection of simulation results, including the expected charge collection efficiency after radiation fluence of $1 \times 10^{15} \text{ n}_{\text{eq}}/\text{cm}^2$ comparable to those expected at HL-LHC (about ten years of running, with an integrated luminosity of 3000 fb^{-1}) for the outer pixel layers. We show that, after irradiation, more than 50 % of the signal should be collected in the edge region; this confirms the validity of the active edge approach.

Keywords: Fabrication technology, TCAD simulations, Planar silicon radiation detectors

*corresponding author

1. Introduction

Planar pixel sensors are nowadays the standard choice for particle tracking and vertex reconstruction in high energy physics experiments. The ATLAS collaboration will upgrade its current Pixel Detector [1] in two phases: in 2013-2014 an additional 4th pixel layer will be inserted (Insertable B-Layer, IBL) [2], while for the High Luminosity phase of LHC (HL-LHC) [3] (beyond 2020) a completely new Pixel Detector is envisaged. The innermost layer of the new pixel sensors will integrate a fluence of about $10^{16} \text{ n}_{\text{eq}}/\text{cm}^2$ for an integrated luminosity of 3000 fb^{-1} , with an instantaneous luminosity of $10^{35} \text{ cm}^{-2} \text{ s}^{-1}$. These harsh conditions demand radiation-hard devices and a finely segmented detector to cope with the expected high occupancy. Several options are under investigation for the upgrade of the ATLAS pixel detector, including diamond [4], silicon 3D [5], HV-CMOS [6] and planar sensors [7].

The new pixel sensors will need to have high geometrical acceptance: the future material budget restrictions and tight mechanical constraints require a geometry inefficiency below 2.5% [2]. For example, the inactive areas at the device periphery should be less than $450 \text{ }\mu\text{m}$ wide for IBL sensors [2]. In conventional sensor designs there is a relatively large un-instrumented area at the edge of the sensor to prevent the electric field from reaching the rim, where a large number of defects are present due to the wafer cutting; for example the current ATLAS pixel sensor has an un-instrumented region of 1.1 mm at the edge [1], including Guard Rings (GRs) and providing a suitable safety margin. GRs, placed all around the pixel area, can help to improve the voltage-handling capability.

One way to reduce or even eliminate the insensitive region along the device periphery is offered by the “active edge” technique, in which a deep vertical trench is etched along the device periphery throughout the entire wafer thickness, thus performing a damage free cut (this requires using a support wafer, to prevent the individual chips from getting loose). The trench is then heavily doped, extending the ohmic back-contact to the lateral sides of the device: the

31 depletion region can then extend to the edge without causing a large current
32 increase. This is the technology we have chosen for realizing n-on-p pixel sensors
33 with reduced inactive zone.

34 Since high voltage is required after heavy irradiation to maintain a deep
35 depletion region and to ensure efficient charge collection in the presence of trap-
36 ping effects, several GRs are commonly used. However, adding one or more GRs
37 spoils the gain of the active behavior of the sensor edge. Indeed, once carriers
38 are created in the guard ring area, or even outside, electrons are collected by
39 the guard rings, which, being floating, re-emit the charge toward all the pixels
40 facing them. Such charge, being distributed among a large number of pixels,
41 beyond the fact that in each pixel it is well below the detection threshold, can-
42 not give any information about the hit position. A compromise should be found
43 between minimization of pixel to trench distance and presence of one or more
44 GRs. In order to gain a better insight into this point, detectors with different
45 termination structures, with and without GRs, have been simulated, designed
46 and fabricated.

47 In this paper the active edge technology (Section 2) is presented; it has
48 been chosen for a first production of n-on-p planar sensors (Section 3). Studies
49 performed with TCAD simulation tools (Section 4) helped in defining the layout
50 and making a first estimation of the charge collection efficiency expected after
51 irradiation.

52 **2. The active edge sensor fabrication at FBK**

53 The sensors are fabricated on 100 mm diameter, high resistivity, p-type,
54 Float Zone (FZ), $\langle 100 \rangle$ oriented, 200 μm thick wafers. The active edge tech-
55 nology [8] is used, which is a single sided process, featuring a doped trench,
56 extending all the way through the wafer thickness, and completely surrounding
57 the sensor. For mechanical reasons, a support wafer is therefore needed, making
58 the back inaccessible after wafer-bonding. Thus, as first process steps, a uni-
59 form high-dose boron implant has been performed on the back side, followed by

60 a thermal oxide growth on both sides.

61 The wafers have then been shipped to Sintef [9], to be wafer-bonded to
62 a 500 μm thick silicon substrate. After having received back the wafers, the
63 remaining process has been performed in the FBK clean-room. A solution will
64 be identified to remove the support wafer and separate the devices; for the time
65 being all the detectors have been designed in order to allow conventional saw-
66 cut separation and substrate biasing from the front-side, through a dedicated
67 ohmic contact (“bias tab”) . In this way, the efficiency of the edge region before
68 and after irradiation can be studied even without removing the support wafer.

69 Up to the trench definition, the process follows quite standard steps. Since
70 the read-out electrodes are n-type, they will be shorted together by the electron
71 inversion layer, induced by the positive fixed charge present in the oxide, unless
72 a p-type implant, compensating such charge, surrounds the pixels. Both ho-
73 mogeneous (“p-spray”) and patterned (“p-stop”) implants have been used; the
74 process splittings adopted in the fabrication batch only concern the presence
75 and the doses of these implants, as detailed in table 1. Electrical tests on irra-
76 diated devices will tell which combination can better guarantee both junction
77 isolation and high breakdown voltages (which are competing demands, since
78 they are in favor of high and low boron doses, respectively), even after years of
79 operation in a harsh radiation environment.

p-spray	p-stop
low dose	absent
high dose	absent
low dose	present
high dose	present
absent	present

Table 1: List of the different isolation solutions adopted in the process.

80 Two patterned high dose implants, a phosphorus implant forming the pixel
81 and GR junctions and a boron implant for the ohmic contact to the substrate

82 (“bias tab”), are then performed.

83 The etching of the trench is accomplished by a Deep Reactive Ion Etching
84 (DRIE) machine (Alcatel AMS-200), the same used for the fabrication of 3D
85 detectors [10]. In the latter case, a 10 μm diameter and 200 μm deep hole has
86 to be etched; the etching mask is made by multiple stacks of dielectrics (oxide
87 and nitride) plus a thick photoresist.

88 The trenches in an active edge sensor must be fully passing, *i.e.* their bottom
89 has to reach the silicon oxide, which separates the active wafer from the support
90 wafer. In the etching of a trench, a problem arises from the fact that the
91 photoresist tends to wear out and/or lift along the sides of the trench, and then
92 to be a less effective mask. Thicker stacks of dielectrics are thus needed.

93 After the trench is etched, its walls are boron-doped in a diffusion furnace.
94 Thus, a continuous ohmic contact to the substrate is created on the trench wall
95 and to the backside. FBK technology can routinely obtain very uniform, well
96 defined and narrow trenches, as shown for example in Figure 1.

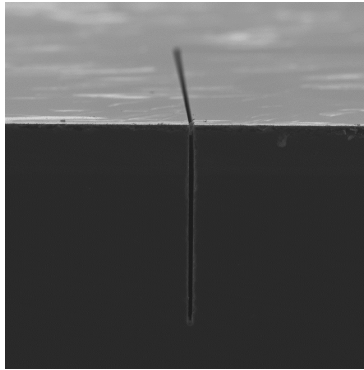


Figure 1: SEM picture of a test trench, after cleaving the wafer perpendicularly to the surface and to the trench itself.

97 The trenches are then oxidized and filled with polysilicon. The remaining
98 processing, arriving at the final device, whose cross-section is sketched in Fig-
99 ure 2, is quite standard, and includes the following steps:

- 100 • contact opening

- metal deposition and patterning
- deposition of a passivation layer (PECVD oxide) and patterning of the same in the pad and bump-bonding regions.

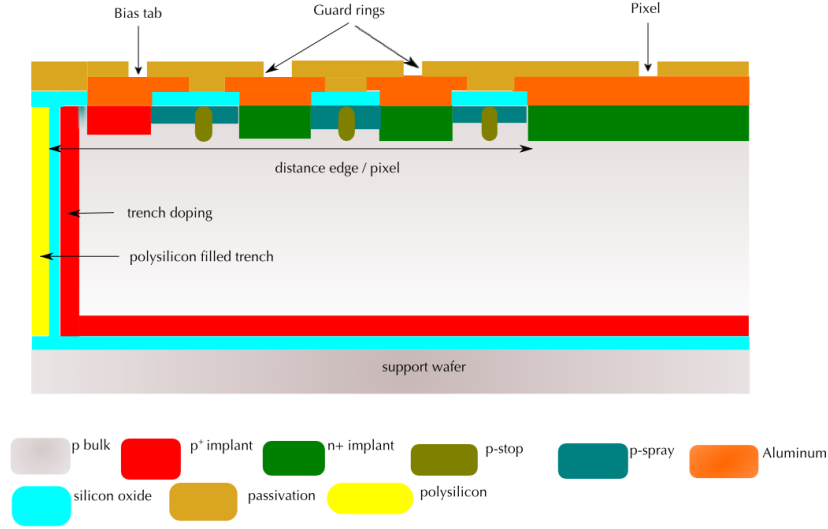


Figure 2: Schematic section of the pixel sensor. The region close to the sensor's edge is portrayed, including the pixel closest to the edge, the edge region, including GRs (when present), the bias tab (present only on one edge of the device), the vertical doped trench, and the support wafer.

Since some sensors will be bump-bonded to FE-I4 [11] read-out chips, it is necessary to select good sensors at the wafer level, by measuring their I-V characteristics. For this purpose, an additional layer of metal is deposited over the passivation and patterned into stripes, each of them shorting together a row of pixels, contacted through the small passivation openings foreseen for the bump bonding. This solution has already been adopted for the selection of good 3D FE-I4 sensors for the ATLAS IBL [13]. After the automatic current-voltage measurement on each FE-I4 sensor, the metal will be removed by wet etching, which does not affect the electrical characteristics of the devices.

113 3. The wafer layout

114 In a 100 mm wafer, there is room for nine FE-I4 compatible pixel sensors; a
 115 detail of one of them is shown in Figure 3.

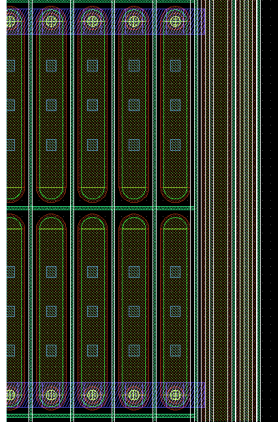


Figure 3: Layout of a detail of an FE-I4 compatible pixel array.

116 FE-I4 compatible pixel sensors consist of an array of 336×80 pixels, at a
 117 pitch of $50 \mu\text{m} \times 250 \mu\text{m}$, for an overall sensitive area of $16.8 \text{ mm} \times 20.0 \text{ mm}$.

118 The nine FE-I4 sensors differ in the pixel-to-trench distance (100, 200, 300,
 119 and $400 \mu\text{m}$) and in the number of the guard rings (0, 1, 2, 3, 5, and 10)
 120 surrounding the pixel area (see Figure 2). The sensor with 3 GRs and a $200 \mu\text{m}$
 121 pixel-to-trench distance features two different GR designs; moreover, two sensors
 122 per each design are present on the wafer. A list of the different FE-I4 sensor
 123 versions is reported in Table 2.

124 A bias tab for substrate biasing (either by probing or by wire bonding),
 125 located internally to the surface delimited by the trench, is placed at about
 126 1.5 mm from the pixelated area on one of the sides (see also Figure 2).

127 The wafer layout also includes four sensors compatible with the FE-I3 read-
 128 out chip [12] (array of 160×18 pixels at a pitch of $50 \mu\text{m} \times 400 \mu\text{m}$, for an overall
 129 area of about $8 \text{ mm} \times 7.2 \text{ mm}$). The trench-pixel distance is $100 \mu\text{m}$ for all of
 130 them, while they differ in the number of GRs (1 or 2). In addition, four sensors

# of GRs	pixel-to-trench distance (μm)
0	100
1	100
2	100
3	200
5	300
10	400

Table 2: List of FEI4 sensors. Two different designs are envisaged for the sensor with 3 GRs and 200 μm pixel-to-trench distance. See text for more details

compatible with the OmegaPIX readout chip [14] are present (array of 96×24 pixels at a pitch of $35\mu\text{m} \times 200\mu\text{m}$, for an overall area of about $3.4 \text{ mm} \times 4.8 \text{ mm}$).

At the periphery of the wafer, there is room for a large number of test structures, *i.e.* square diodes and small arrays of FE-I4-like pixels, which differ in the number of GRs surrounding the active area and in the trench-to-pixel distance. Several possible combinations have been implemented, including all those used for the FE-I4 sensors. The aim of these structures is to test the isolation and to measure the high-voltage behavior before and (possibly) after irradiation, in order to find the best sensor configuration to be bump-bonded to the read-out chip and to select the best combination of GR number and trench distance for a possible future production.

To study the charge collection properties of the sensors, particularly in the edge region, “stripixel” arrays have also been designed. They are small 1-D arrays of about 2 mm long strips, which are an elongated version of the FE-I4 pixels with the addition of a pad at one end, so that they can be wire bonded to a readout chip for strip detectors. Also in this case, there are several combinations of trench distances and number of GRs.

149 4. TCAD simulation

150 In order to explore and compare the properties of the design variations
 151 considered, numerical simulations were performed with TCAD tools from SIL-
 152 VACO [15]. 2D structures analogous to the one sketched in Figure 2 have been
 153 simulated, varying parameters like the number of GRs and the pixel-to-trench
 154 distance. The break down (BD) behaviour of the devices, the electrical field
 155 distribution and the charge collection efficiency (CCE) were studied, for simu-
 156 lated un-irradiated and irradiated sensors, with a fluence $\phi = 1 \times 10^{15} \text{ n}_{\text{eq}}/\text{cm}^2$.
 157 This is the expected fluence for the outer pixel layers of the new tracker at the
 158 end of the HL-LHC phase.

159 In the following, details on dopant parameterization, on device physics mod-
 160 els adopted and on the radiation damage parameterization will be presented,
 161 followed by a selection of results from simulations.

162 4.1. Doping parameters

163 Each of the doped regions (n^+ for the pixel and the GRs, p^+ for the backside,
 164 p-stop, p-spray, bias tab and the trench walls) have been modeled with simple
 165 functions, depending on a set of parameters like the peak concentration, the
 166 reference concentration, *i.e.* the concentration value at a distance equal to the
 167 rolloff from the peak position, and the vertical rolloff distance. The values used
 168 are summarized in Table 3.

Doped region	impurity	function	peak value (cm^{-3})	reference value (cm^{-3})	rolloff (μm)
Pixel and GR	D	gaussian	2×10^{19}	10^{16}	1.0
Back	A	gaussian	2×10^{19}	10^{16}	1.0
Trench	A	erf	2×10^{19}	10^{12}	2.0
Bias tab	A	gaussian	2×10^{19}	2×10^{16}	0.5
P-spray	A	gaussian	5×10^{16}	7×10^{15}	0.5
P-stop	A	gaussian	5×10^{17}	7×10^{16}	0.5

Table 3: Implant parameters for simulated detectors; A (D) is for acceptor (donor) impurities.

169 *4.2. Physics models and radiation damage parameterization*

170 SILVACO TCAD uses a complete set of physical models for semiconduc-
 171 tor device simulation. Among them, models for concentration dependent mo-
 172 bility, field dependent mobility, bandgap narrowing, concentration dependent
 173 lifetime, trap-assisted and Auger recombination were used. Oxide fixed charge
 174 density (with surface density $Q_{\text{ox}} = 10^{11}/\text{cm}^2$ before irradiation, and $Q_{\text{ox}} =$
 175 $3 \times 10^{12}/\text{cm}^2$ after), generation-recombination lifetimes and surface recombina-
 176 tion velocity have been set according to measured IV and CV characteristics of
 177 diodes from previous n-on-p SiS^1 productions.

178 The defects at the edge have been modeled with a $1 \mu\text{m}$ wide region in which
 179 the generation-recombination lifetime was set to a very small value (10^{-12} s; for
 180 comparison, before irradiation the corresponding value for the bulk is of 10^{-5} s).
 181 If the trench doping were not effective, a large current would appear as soon as
 182 the electric field reaches the edge area.

183 To describe the radiation damage, an effective model based on three deep
 184 levels in the forbidden gap was used [16]. Each of these deep levels is defined
 185 as either donor (D) or acceptor (A), and is characterized by its energy (with
 186 respect to the closest energy band), its capture cross-sections for electrons (σ_e)
 187 and holes (σ_h) and its introduction rate η , which is the proportionality term
 188 between defect concentration and radiation fluence. In Table 4 these properties
 189 are summarized.

Type	Energy (eV)	$\sigma_e(\text{cm}^2)$	$\sigma_h(\text{cm}^2)$	$\eta(\text{cm}^{-1})$
A	$E_C - 0.42$	9.5×10^{-15}	9.5×10^{-14}	1.613
A	$E_C - 0.46$	5.0×10^{-15}	5.0×10^{-14}	0.9
D	$E_V + 0.36$	3.23×10^{-13}	3.23×10^{-14}	0.9

Table 4: Relevant parameters for acceptors (A) and donor (D) deep levels in the bandgap, describing the radiation damage.

¹Forschungsinstitut für Mikrosensorik und Photovoltaik GmbH

190 The deep level close to the centre of the bandgap is an highly effective
 191 generation center affecting the leakage current, while the other two contribute
 192 to the change of the effective doping concentration of the bulk and hence the
 193 depletion voltage.

194 Radiation-induced interface traps at the Si-SiO₂ interface are also included
 195 in the simulation, as described in [17].

196 The model was validated by comparing simulation results to the change in
 197 depletion voltage and leakage current in irradiated n-on-p diodes from previous
 198 productions.

199 4.3. Simulation results

200 The structure in Figure 2 was slightly modified in the simulations: the sup-
 201 port wafer was not present and the backside p⁺ implant was metallized. This
 202 was done in order to simulate a sensor ready for use.

203 The sensors were simulated under reverse bias, applying a negative voltage
 204 to the back contact while keeping the pixel at ground potential; the bias tab was
 205 left floating. Different geometries were simulated, varying the number of GRs
 206 and the pixel-to-trench distance; see Table 5 for the list of simulated geometries.
 207 If present, the GRs were left floating during the simulations.

# of GRs	pixel-to-trench distance (μm)
0	100
1	100
2	100
0	200
1	200
2	200

Table 5: List of simulated sensor layouts.

208 *Current-voltage characteristic and break down voltage*

209 Figure 4 shows the current-voltage curves of all the simulated designs, before
 210 irradiation. The depletion voltage has been estimated using AC analysis for
 211 simulations, determining the depletion voltage value from the fit to the $\log(C)$ –
 212 $\log(V)$ curve; the result was checked against the aforementioned measurements
 213 on n-on-p diodes from a former production. A sensor with a design compatible
 214 with the current ATLAS pixel modules was also simulated; it features a pixel-
 215 to-trench distance of 1.1 mm and 16 GRs.

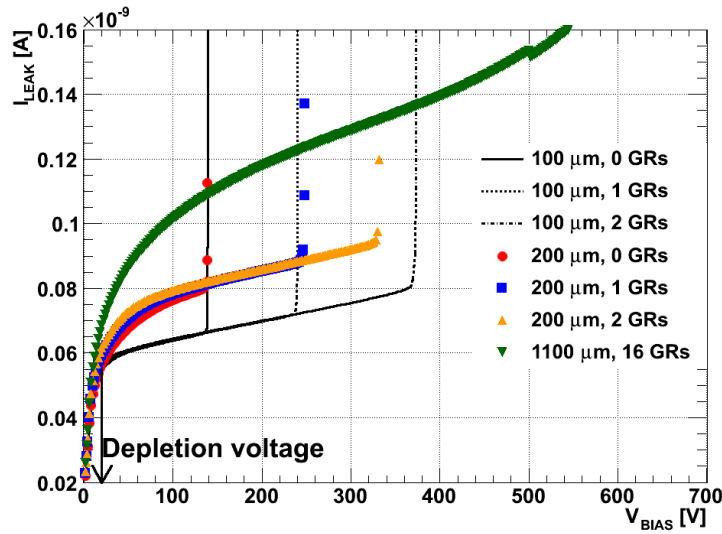


Figure 4: Simulated IV curves for the pixel closest to the edge, for several sensor designs before irradiation (see text for details). The simulated current has been scaled to reproduce the behaviour of a $50\ \mu\text{m}$ wide pixel in the edge direction. The depletion voltage is indicated by the arrow.

216 From Figure 4 it can be seen that before irradiation the BD voltage exceeds
 217 by at least 100 V the depletion voltage for all the designs we considered. The
 218 ATLAS-like sensor shows higher BD voltage with respect to those predicted
 219 for our edgeless detectors, but all sensors are largely over-depleted before BD.
 220 Increasing the pixel-to-trench distance yields a higher bulk-generated current,

221 since the depleted volume can further extend laterally. Adding more GRs helps
 222 greatly in increasing the value of BD voltage, extending the operability range
 223 of the sensors. The best performance is obtained from a device with 2 GRs and
 224 a $100\mu\text{m}$ pixel-to-trench distance.

225 As reported in the literature by different groups (*e.g.* [19]), after irradiation
 226 the BD voltage increases to much larger values. Our simulations of irradiated
 227 devices confirm this observation, as it can be seen in Figure 5 where the same set
 228 of sensors of Figure 4 is now presented after a simulated fluence of $10^{15}\text{n}_{\text{eq}}/\text{cm}^2$.
 229 No BD is observed in any sensor up to 1000 V bias voltage.

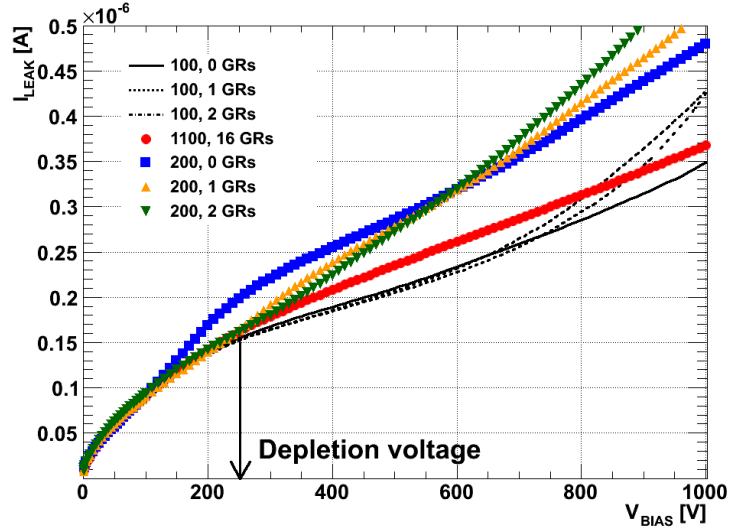


Figure 5: Simulated IV curves for the pixel closest to the edge, for several sensor designs after a simulated fluence of $10^{15}\text{n}_{\text{eq}}/\text{cm}^2$ (see text for details). The simulated current has been scaled to reproduce the behaviour of a $50\mu\text{m}$ wide pixel in the edge direction. The depletion voltage is indicated by the arrow.

230 *Electric field distribution*

231 In Figure 6 the electric field distribution is shown for an un-irradiated de-
 232 tector with 2 GRs and $100\mu\text{m}$ pixel-to-trench distance, for a bias voltage of
 233 50 V.

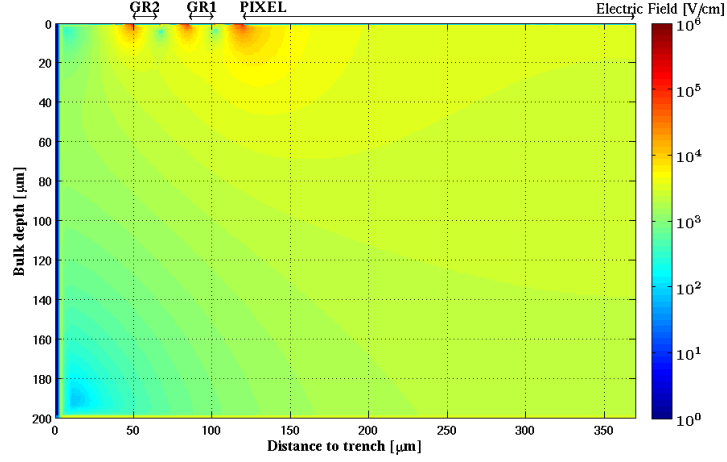


Figure 6: Electric field distribution for non-irradiated device at $V_{\text{bias}} = 50$ V. The sensor has 2 GRs with a $100 \mu\text{m}$ distance between trench and pixel.

234 It can be seen that the detector is fully depleted and the electric field is
 235 maximum in the region of the p-stops, with a value of some units in 10^4V/cm .
 236 It can also be observed that the electric field in the edge region is non negligible,
 237 hence signal should be collectable from there.

238 In Figure 7 the electric field distribution is reported for a sensor with 2 GRs
 239 and $100 \mu\text{m}$ pixel-to-trench distance, after a simulated fluence $\phi = 10^{15} \text{n}_{\text{eq}}/\text{cm}^2$.

240 In Figure 7, top, the detector is biased at 50 V; a large portion of the volume
 241 is non-depleted, *i.e.* the electric field is negligible. An interesting feature is an
 242 increase of the high electric field close to the back implant and to the trench:
 243 this is a known effect called double peak (DP) [18]. The fact that it is accounted
 244 for by our simulation supports the reliability of the simulation itself.

245 In Figure 7, bottom, the electric field distribution is reported for the same
 246 irradiated detector at a bias voltage of 400 V, well beyond the depletion volt-
 247 age (~ 250 V). The electric field extends all over the bulk, although a small
 248 undepleted region is still present at the edge, near the back-side; nonetheless,
 249 a large portion of the region between the pixel and the trench shows a sizable
 250 electric field, confirming the possibility of charge collection in the edge region,

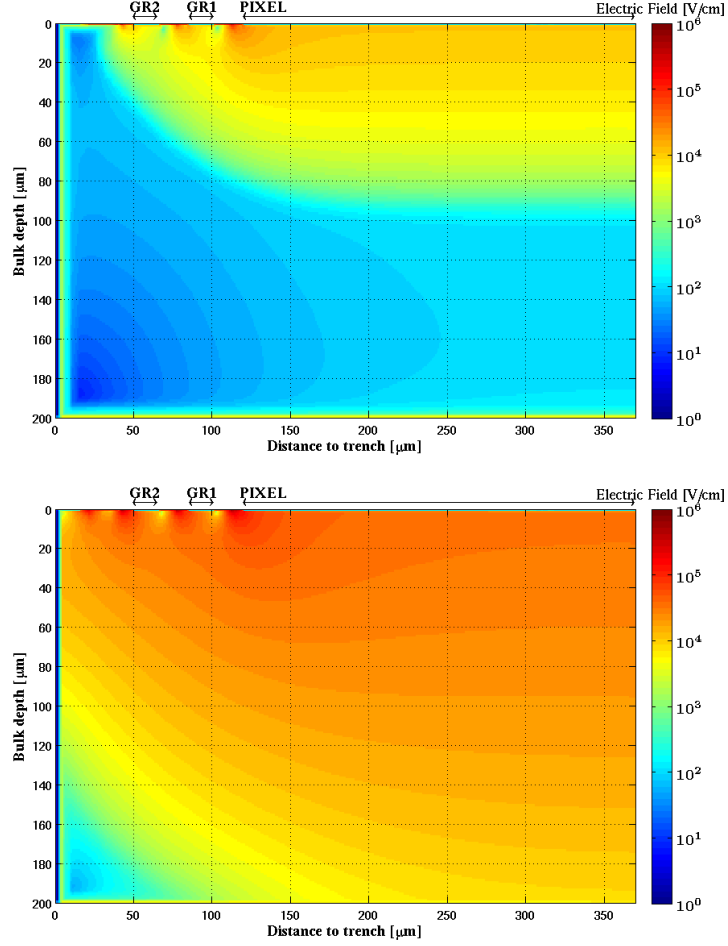


Figure 7: Electric field distributions for a device irradiated with a fluence $\phi = 10^{15} \text{ n}_{\text{eq}}/\text{cm}^2$. Top: $V_{\text{bias}} = 50 \text{ V}$; bottom: $V_{\text{bias}} = 400 \text{ V}$. The sensor has 2 GRs and a $100 \mu\text{m}$ distance between edge and pixel.

251 after irradiation too. As before irradiation, the electric field is maximum in the
 252 region of the p-stops, but now its value is in the 10^5 V/cm range.

253 *Charge collection efficiency*

254 To study charge collection efficiency (CCE) after irradiation, charge creation
 255 in irradiated sensors was simulated. The most interesting case is when the

charge is released in the gap between the pixel and the trench, when no GRs are present. If a significant amount of charge can be collected after irradiation in that region, the edgeless concept would be verified to work.

Our sensor was illuminated from the front side with a simulated 1060 nm laser beam, setting its power in order to generate the same charge that would be released by a minimum ionizing particle (MIP) traversing 200 μm of silicon ($\sim 2.6 \text{ fC}$). The laser beam was originating above the front side of the detector, with a 2 μm wide gaussian beamspot. The duty cycle of the laser was 50 ns, with the power ramping up in 1 ns, remaining constant for 10 ns and ramping down in the next nanosecond.

The CCE was studied as a function of the bias voltage for the detector with no GRs and a 100 μm trench-to-pixel distance. Two incidence points of the laser beam have been considered: one within the pixel and the other in the edge region, at 50 μm distance from the pixel. In the following they will be identified as “Pixel” and “Edge”, respectively.

Based on the properties of the laser beam and of the target material, the simulation program determined the charge of carriers photogenerated inside the device by one pulse. The charge collected by the pixel was defined as the integral over the laser duty cycle of the current flowing through the pixel, once the stable leakage current had been subtracted. Finally, the CCE was obtained by dividing this collected charge by the total photogenerated charge.

In Figure 8 the CCE is presented as a function of the bias voltage for the simulated fluence for the two incidence points of the laser beam.

At a fluence $\phi = 10^{15} \text{ n}_{\text{eq}}/\text{cm}^2$ more than 50 % of the signal is collected in the “Edge” region at a bias voltage of 500 V; as a comparison, 70 % of the signal is retained in the “Pixel” region. In both cases the effect of trapping can be observed: the collected charge reaches a *plateau* at high voltage, but there the CCE is not of 100 %. No charge is collected from the “Edge” region below 100 V: indeed at 100 V bias the electric field is negligible in that region when there are no GRs. It can be seen that while the maximum CCE for a charge created in the pixel region is reached at a bias voltage above $\sim 400 \text{ V}$, in the

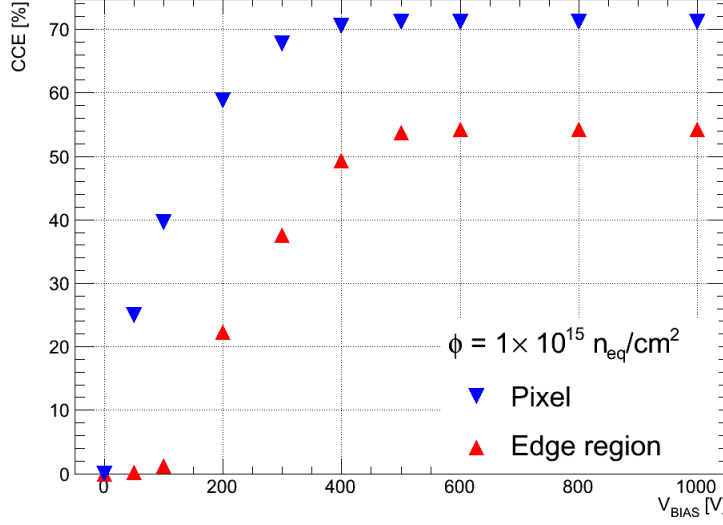


Figure 8: Charge collection efficiency as a function of bias voltage for an irradiated device at a fluence $\phi = 10^{15} \text{ n}_{\text{eq}}/\text{cm}^2$. The laser is entering the detector either in the pixel region (“Pixel”) or in the un-instrumented region (“Edge region”). The sensor has no GRs, and a $100 \mu\text{m}$ distance between edge and pixel.

287 “Edge” region a bias voltage of 600 V is needed: this is consistent with the
 288 depletion zone extending laterally.

289 Calculations based on trapping time experimental data [20] for our sensor
 290 thickness and our target fluence produce CCE estimations in agreement with
 291 our simulations.

292 5. Conclusions and outlook

293 In view of the Large Hadron Collider High Luminosity (HL-LHC) phase, an
 294 upgrade of the ATLAS Inner Detector is envisaged. New pixel sensors will have
 295 to work in an unprecedentedly harsh environment; moreover, material budget
 296 restrictions and tight mechanical constraints demand for a reduction of the
 297 inactive region at the edge of sensors.

298 FBK Trento and LPNHE Paris are developing new planar n-on-p pixel sen-
 299 sors for the ATLAS detector upgrade, characterized by a reduced inactive region
 300 at the edge thanks to a vertical doped lateral surface at the device boundary,
 301 the “active edge” technology. Simulation studies show the effectiveness of this
 302 technique in reducing the dead area while retaining a large margin of operabil-
 303 ity in terms of bias voltage, even after simulated fluences comparable to those
 304 expected at the end of the HL-LHC phase for the external layers; they also
 305 show that after irradiation more than 50 % of the signal is retained, even in the
 306 “Edge” region.

307 Next steps will be a full electrical characterization of these “active edge”
 308 devices, followed by functional tests of the pixel sensors with radioactive sources
 309 and eventually in a beam test, after having bump bonded a number of pixel
 310 sensors to the FE-I4 read out chips.

311 Acknowledgements

312 The authors would like to express their gratitude to E. Fretwurst for his
 313 useful discussions. The fabrication of the detectors was supported by INFN.

314 References

- 315 [1] The ATLAS collaboration, JINST 3 P07007, 2008
- 316 [2] ATLAS TDR 19, CERN/LHCC 2010-013,
 317 <http://cdsweb.cern.ch/record/1291633/files/ATLAS-TDR-019.pdf>
- 318 [3] M. Lamont, <http://dx.doi.org/10.3204/DESY-PROC-2010-01/8>
- 319 [4] D. Asner *et al.*, Nucl. Instr. and Meth. A 636 (2011) 125-129
- 320 [5] P. Hansson *et al.*, Nucl. Instr. and Meth. A 628 (1) (2011) 216 - 220
- 321 [6] I. Peric, JINST 7 C08002, 2012
- 322 [7] M. Bomben *et al.*, Physics Procedia 37 (2012) 940 - 949

- 323 [8] C. J. Kenney *et al.*, IEEE Trans. Nucl. Sci. NS-48 (6) (2001) 2405.
- 324 [9] SINTEF,
325 Stiftelsen SINTEF, box 4760 Sluppen, NO-7465 TRONDHEIM, NORWAY
- 326 [10] C. Da Via *et al.*, Nucl. Instr. and Meth. A 694 (2012) 321 - 330
- 327 [11] M. Garcia-Sciveres *et al.*, Nucl. Instr. and Meth. A 636 (2011) S155-S159.
- 328 [12] I. Perić *et al.*, Nucl. Instr. and Meth. A 565 (2006) 178 - 187.
- 329 [13] E. Vianello *et al.*, Nuclear Science Symposium and Medical Imaging Con-
330 ference (NSS/MIC), 2011 IEEE (2011), 523-528
- 331 [14] *OmegaPIX*
- 332 [15] *Silvaco, Inc.*
333 4701 Patrick Henry Drive, Bldg 2
334 Santa Clara, CA 95054
- 335 [16] D. Pennicard *et al.*, Nucl. Instr. and Meth. A 592 (2008) 16-25.
- 336 [17] J. Schwandt *et al.*, JINST 7 C01006, 2012
- 337 [18] V. Chiochia *et al.*, Nucl. Instr. and Meth. A 568 (2006) 51-55.
- 338 [19] P. Weigell *et al.*, Nucl. Instr. and Meth. A 658 (2011) 36-40.
- 339 [20] G. Kramberger *et al.*, Nucl. Instr. and Meth. A 476 (2002) 645-651.